An Immersed Boundary Method for a Contractile Elastic Ring in a Three-Dimensional Newtonian Fluid

Seunggyu Lee, Darae Jeong, Wanho Lee & Junseok Kim

Journal of Scientific Computing

ISSN 0885-7474
Volume 67
Number 3

J Sci Comput (2016) 67:909-925
DOI 10.1007/s10915-015-0110-8

Springer

J Sci Comput (2016) 67:909–925
DOI 10.1007/s10915-015-0110-8

An Immersed Boundary Method for a Contractile Elastic Ring in a Three-Dimensional Newtonian Fluid

Seunggyu Lee[1] · **Darae Jeong**[1] · **Wanho Lee**[2] · **Junseok Kim**[1]

Received: 29 April 2015 / Revised: 15 September 2015 / Accepted: 16 September 2015 /
Published online: 22 September 2015

Abstract In this paper, we present an immersed boundary method for modeling a contractile elastic ring in a three-dimensional Newtonian fluid. The governing equations are the modified Navier–Stokes equations with an elastic force from the contractile ring. The length of the elastic ring is time dependent and the ring shrinks with time because of its elastic nature in our proposed model. We dynamically reduce the number of Lagrangian boundary points when the distance between adjacent points is too small. This point-deleting algorithm helps keep the number of immersed boundary points in a single Cartesian mesh grid from becoming too high. We perform numerical experiments with various initial configurations of the contractile elastic ring, and numerical simulations to investigate the effects of the parameters are also conducted. The numerical results show that the proposed method can model and simulate the time-dependent contractile elastic ring in a three-dimensional Newtonian fluid.

Keywords Immersed boundary method · Contractile elastic ring · Navier–Stokes equation · Multigrid method

1 Introduction

Cell division is one of the most important behaviors of living cells. However, its general principles are still not clear because of its complicated process and various lineages in each cytokinesis gene [1]. The process of physical cell division is caused by the contractile ring (CR) on the cell membrane. The main protein content of the ring in eukaryotes is actin filaments and myosin motors, which cluster on the membrane and produce a contractile force (see [2] and references therein).

✉ Junseok Kim
cfdkim@korea.ac.kr

1 Department of Mathematics, Korea University, Seoul 136-713, Republic of Korea

2 National Institute for Mathematical Sciences, Daejeon 305-811, Republic of Korea

We are motivated to model and simulate three-dimensional cell growth and division. Many studies of the the function of the CR during cytokinesis have been published [3–12], as one of the key elements in modeling cell division is how to model and simulate the CR. Nevertheless, the detailed assembly and dynamics of the CR in cells are poorly understood [13]. The authors in [14] proposed a simple numerical model of one hypothesis for the assembly mechanism of the CR in cytokinesis by fission yeast using the Monte Carlo method. Zhou et al. [15] recently showed that a function of the CR is to spatially coordinate curvature-dependent septum assembly during fission yeast cytokineses.

In this paper, we focus on modeling and simulation of the CR in a three-dimensional incompressible Newtonian fluid using the immersed boundary (IB). The IB method was originally developed by Peskin to study the fluid dynamics of blood flow in the human heart [16–18] and has been successfully applied to many problems [19–23].

There have been a number of simulations of an elastic boundary using the IB method [24–29]. One of the advantages of the IB method is that we can solve the Navier–Stokes equations on a single Cartesian domain where flexible boundaries were enabled to move or change shapes in a complicated fashion [30]. Lim et al. [24,25] studied the dynamics of a bent, twisted, and closed circular rod in a viscous incompressible fluid using a generalized version of the IB method combined with the nonstandard Kirchhoff rod theory. Vahidkhah and Abdollahi [26] considered the interactions between a deformable fiber and a viscous channel flow. Deformation of a massless elastic fiber was simulated numerically using the IB-lattice Boltzmann method.

This paper is organized as follows. In Sect. 2, we describe the mathematical model for a contractile elastic ring in a three-dimensional Newtonian fluid. In Sect. 3, we describe the discretization of the governing equations and present numerical solution algorithms. Numerical experiments are presented in Sect. 4. Finally, our conclusion is given in Sect. 5.

2 Mathematical Model

We consider a closed contractile elastic ring immersed in a three-dimensional incompressible fluid. The equations of fluid motion are given as

$$\rho\left(\frac{\partial \mathbf{u}}{\partial t}+\mathbf{u}\cdot\nabla\mathbf{u}\right)=-\nabla p+\eta\Delta\mathbf{u}+\mathbf{f},\quad \text{in } \Omega\times(0,\infty), \tag{1}$$

$$\nabla\cdot\mathbf{u}=0, \tag{2}$$

where $\mathbf{u}(\mathbf{x},t)=(u(\mathbf{x},t),v(\mathbf{x},t),w(\mathbf{x},t))$ is the velocity, $p(\mathbf{x},t)$ is the pressure, $\mathbf{x}=(x,y,z)$ is the Cartesian coordinate on $\Omega=(a,b)\times(c,d)\times(e,f)\subset\mathbb{R}^3$, t is the time variable, ρ is the density, and η is the viscosity. Here, the no-slip boundary condition is applied. The fluid force density $\mathbf{f}(\mathbf{x},t)$ is given as

$$\mathbf{f}(\mathbf{x},t)=(f_1(\mathbf{x},t),f_2(\mathbf{x},t),f_3(\mathbf{x},t))=\int_0^{L_t}\mathbf{F}(s,t)\delta(\mathbf{x}-\mathbf{X}(s,t))\mathrm{d}s, \tag{3}$$

where s is a parameter, $\delta(\mathbf{x})$ is a three-dimensional smoothed Dirac-delta function, and $\mathbf{X}(s,t)=(X(s,t),Y(s,t),Z(s,t))$ is the Lagrangian variable of the CR. Here $0\le s\le L_t$, where L_t is the unstressed length of the boundary. Note that it is periodic with respect to s, i.e., $\mathbf{X}(0,t)=\mathbf{X}(L_t,t)$. To model the shrinking of the CR, we let L_t be time-dependent length. The CR has an elastic force that enables it to be dynamically shortened from the time-dependent L_t. The elastic force density $\mathbf{F}(s,t)$ generated by the ring is derived from

the elastic stretching energy at the rest length [31]:

$$E(\mathbf{X}(s,t)) = \frac{\sigma}{2}\int_0^{L_t}\left(\left|\frac{\partial \mathbf{X}}{\partial s}\right| - 1\right)^2 \mathrm{d}s, \tag{4}$$

where σ is the stiffness constant for the ring and $|\mathbf{X}| = \sqrt{X^2 + Y^2 + Z^2}$ is the L_2-norm. From the variation of the energy functional $\wp E$, we define $\mathbf{F}(s,t)$ as the negative of the variational derivative:

$$\wp E(\mathbf{X}(s,t)) = -\int_0^{L_t} \mathbf{F}(s,t)\cdot \wp\mathbf{X}(s,t)\mathrm{d}s, \tag{5}$$

where $\wp$ is a variation symbol, which distinguishes the symbol from the Dirac delta function [18]. From the expression for the elastic energy, we obtain

$$\begin{aligned}\wp E(\mathbf{X}(s,t)) &= \frac{d}{d\theta}E(\mathbf{X}+\theta\wp\mathbf{X})\Big|_{\theta=0}\\ &= \sigma\int_0^{L_t}\left(\left|\frac{\partial \mathbf{X}}{\partial s}\right| - 1\right)\frac{\partial \mathbf{X}/\partial s}{|\partial \mathbf{X}/\partial s|}\cdot\frac{\partial(\wp\mathbf{X})}{\partial s}\mathrm{d}s\\ &= -\sigma\int_0^{L_t}\frac{\partial}{\partial s}\left[\left(\left|\frac{\partial \mathbf{X}}{\partial s}\right| - 1\right)\frac{\partial \mathbf{X}/\partial s}{|\partial \mathbf{X}/\partial s|}\right]\cdot\wp\mathbf{X}\mathrm{d}s,\end{aligned} \tag{6}$$

where we have used integration by parts and the periodicity of s. Comparing Eqs. (5) and (6), we define the elastic force density as $\mathbf{F}(s,t) = \dfrac{\partial}{\partial s}\left[T(s,t)\boldsymbol{\tau}(s,t)\right]$, where

$$T(s,t) = \sigma\left(\left|\frac{\partial \mathbf{X}}{\partial s}\right| - 1\right) \tag{7}$$

is the tension of the ring and

$$\boldsymbol{\tau}(s,t) = \frac{\partial \mathbf{X}/\partial s}{|\partial \mathbf{X}/\partial s|} \tag{8}$$

is the unit tangent vector to the ring. The evolution equation of the ring is given by

$$\frac{\partial \mathbf{X}(s,t)}{\partial t} = \mathbf{U}(s,t) = \int_\Omega \mathbf{u}(\mathbf{x},t)\delta(\mathbf{x}-\mathbf{X}(s,t))\mathrm{d}\mathbf{x}, \tag{9}$$

where $\mathbf{U}(s,t)$ is the boundary velocity on $\mathbf{X}(s,t)$.

3 Numerical Solution Algorithm

In this section, we describe the discretization of the governing Eqs. (1), (2), and (9). To simplify the exposition, we consider the equations on the unit cube computational domain $\Omega = (0,1)^3$. Let h be the uniform mesh grid size, then the center of the cell is $\mathbf{x}_{ijk} = (x_i, y_j, z_k) = ((i-0.5)h, (j-0.5)h, (k-0.5)h)$ for $i, j, k = 1, \ldots, N$. Here, N denotes the number of grid points in each direction. Let Δt be the time step size. To discretize the equations, a staggered marker-and-cell (MAC) mesh [32] is used; i.e., the pressure $p(\mathbf{x},t)$ is stored at the cell-centers and the velocity components $u(\mathbf{x},t)$, $v(\mathbf{x},t)$, and $w(\mathbf{x},t)$ are stored at the cell-edges. In a discretized equation, we denote $p(\mathbf{x}_{ijk}, n\Delta t)$ as p^n_{ijk}. By discretizing

the non-dimensionalized versions of Eqs. (1) and (2), we can rewrite them as follows:

$$\frac{\mathbf{u}^{n+1}-\mathbf{u}^n}{\Delta t}+\mathbf{u}^n\cdot\nabla_d\mathbf{u}^n=-\nabla_d p^{n+1}+\frac{1}{Re}\Delta_d\mathbf{u}^n+\frac{1}{We}\mathbf{f}^n, \tag{10}$$

$$\nabla_d\cdot\mathbf{u}^{n+1}=0, \tag{11}$$

where $Re=\rho U^*L^*/\eta$ is the Reynolds number and $We=\rho(U^*)^2L^*/\sigma$ is the Weber number with the characteristic velocity U^* and length L^*. Therefore, in three-dimensional Cartesian coordinates, we have

$$\frac{u^{n+1}_{i+\frac{1}{2},jk}-u^n_{i+\frac{1}{2},jk}}{\Delta t}+(\mathbf{u}\cdot\nabla_d u)^n_{i+\frac{1}{2},jk}=-\frac{p^{n+1}_{i+1,jk}-p^{n+1}_{ijk}}{h}+\frac{1}{Re}\Delta_d u^n_{i+\frac{1}{2},jk}+\frac{1}{We}f^n_{1\,i+\frac{1}{2},jk}, \tag{12}$$

$$\frac{v^{n+1}_{i,j+\frac{1}{2},k}-v^n_{i,j+\frac{1}{2},k}}{\Delta t}+(\mathbf{u}\cdot\nabla_d v)^n_{i,j+\frac{1}{2},k}=-\frac{p^{n+1}_{i,j+1,k}-p^{n+1}_{ijk}}{h}+\frac{1}{Re}\Delta_d v^n_{i,j+\frac{1}{2},k}+\frac{1}{We}f^n_{2\,i,j+\frac{1}{2},k}, \tag{13}$$

$$\frac{w^{n+1}_{ij,k+\frac{1}{2}}-w^n_{ij,k+\frac{1}{2}}}{\Delta t}+(\mathbf{u}\cdot\nabla_d w)^n_{ij,k+\frac{1}{2}}=-\frac{p^{n+1}_{ij,k+1}-p^{n+1}_{ijk}}{h}+\frac{1}{Re}\Delta_d w^n_{ij,k+\frac{1}{2}}+\frac{1}{We}f^n_{3\,ij,k+\frac{1}{2}}, \tag{14}$$

$$(\nabla_d\cdot\mathbf{u})^{n+1}_{ijk}=0. \tag{15}$$

Here, we denote $f^n_{m\,i+\frac{1}{2},jk}=0.5(f^n_{m\,i+1,jk}+f^n_{m\,ijk})$ for $m=1,2,3$. Let Δs^n_l be the time-dependent step sizes satisfying $L_t=\sum_{l=0}^{N_s-1}\Delta s^n_l=\alpha(t^n)L_0$, where L_t is the time dependent length of the CR, N_s is the number of intervals, $\alpha(t^n)$ is a scaling factor function at time $t=t^n$, and L_0 is the initial length of the CR. Then, $s^n_0=0$ and $s^n_{l+1}=s^n_l+\Delta s^n_l$ for $l=0,\ldots,N_s-1$. The CR is defined as $\mathbf{X}^n_l=\mathbf{X}(s^n_l,n\Delta t)=(X^n_l,Y^n_l,Z^n_l)$ for $l=1,\ldots,N_s$. Note that $\mathbf{X}^n_0=\mathbf{X}^n_{N_s}$ and $\mathbf{X}^n_{N_s+1}=\mathbf{X}^n_1$ because of the periodicity. This parametrization of $\mathbf{X}(s,t)$ is schematically illustrated in Fig. 1.

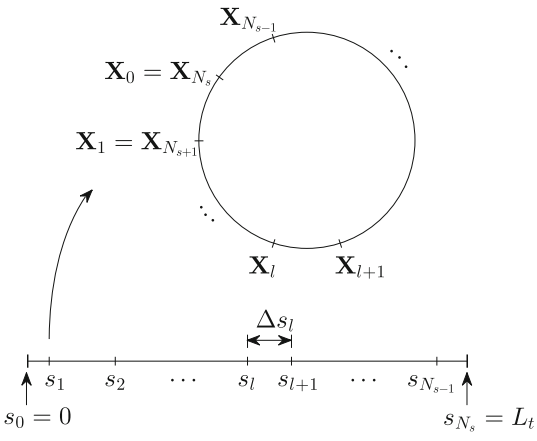

Fig. 1 Schematic of parametrization of $\mathbf{X}(s,t)$

Given $\mathbf{u}^n$ and $\mathbf{X}^n$, we want to find $\mathbf{u}^{n+1}$ and $\mathbf{X}^{n+1}$ by solving Eqs. (10) and (11) using the projection method [33] and Eq. (9).

First, let us calculate the CR force $\mathbf{f}$. Let D_s be the discrete differential operator with respect to s:

$$D_s\mathbf{X}^n_{l+\frac{1}{2}} = \left(X^n_{l+1} - X^n_l, Y^n_{l+1} - Y^n_l, Z^n_{l+1} - Z^n_l\right) / \Delta s^n_l.$$

Then, Eqs. (7) and (8) are discretized as $T^n_{l+\frac{1}{2}} = \sigma\left(\left|D_s\mathbf{X}^n_{l+\frac{1}{2}}\right| - 1\right)$ and $\boldsymbol{\tau}^n_{l+\frac{1}{2}} = D_s\mathbf{X}^n_{l+\frac{1}{2}} \Big/ \left|D_s\mathbf{X}^n_{l+\frac{1}{2}}\right|$, respectively. The ring force density is defined as $\mathbf{F}^n_l = 2(T^n_{l+\frac{1}{2}}\boldsymbol{\tau}^n_{l+\frac{1}{2}} - T^n_{l-\frac{1}{2}}\boldsymbol{\tau}^n_{l-\frac{1}{2}})/(\Delta s^n_{l-1} + \Delta s^n_l)$. Then the cell-centered force $\mathbf{f}$ is given as

$$\mathbf{f}^n(\mathbf{x}) = \sum_{l=l}^{N_s} \mathbf{F}^n_l \delta_h(\mathbf{x} - \mathbf{X}^n_l)\frac{\Delta s^n_{l-1} + \Delta s^n_l}{2}. \tag{16}$$

Here, δ_h is an approximation to the three-dimensional smoothed Dirac-delta function as $\delta_h(\mathbf{x}) = \delta(x/h)\,\delta(y/h)\,\delta(z/h)/h^3$, where a four-point delta function [34] is given by

$$\delta(r) = \begin{cases} \left(3 - 2|r| + \sqrt{1 + 4|r| - 4r^2}\right)/8 & \text{if } |r| \le 1, \\ \left(5 - 2|r| - \sqrt{-7 + 12|r| - 4r^2}\right)/8 & \text{if } 1 < |r| \le 2, \\ 0 & \text{otherwise.} \end{cases} \tag{17}$$

Next, we compute an intermediate velocity field, $\tilde{\mathbf{u}}$, which generally does not satisfy the incompressible condition. To apply the no-slip boundary condition, we set the values of ghost points as $u^n_{-\frac{1}{2},jk} = 0$, $v^n_{0,jk} = -v^n_{1,jk}$, and $w^n_{0,jk} = -w^n_{1,jk}$ in the x-direction. The reason that only u^n has a different type of formula is that only u^n is saved at a cell-edge in the x-direction on the MAC mesh. The values at ghost points in the y- and z-directions are similarly defined. From Eq. (12) without the pressure gradient term, we have

$$\frac{\tilde{u}^{n+1}_{i+\frac{1}{2},jk} - u^n_{i+\frac{1}{2},jk}}{\Delta t} + (\mathbf{u}\cdot\nabla_d u)^n_{i+\frac{1}{2},jk} = \frac{1}{Re}\Delta_d u^n_{i+\frac{1}{2},jk} + \frac{1}{We} f^n_{1\,i+\frac{1}{2},jk}.$$

Then we define

$$\begin{aligned}\tilde{u}^{n+1}_{i+\frac{1}{2},jk} = u^n_{i+\frac{1}{2},jk} &- \Delta t(\mathbf{u}\cdot\nabla_d u)^n_{i+\frac{1}{2},jk} + \frac{\Delta t}{We} f^n_{1\,i+\frac{1}{2},jk} + \frac{\Delta t}{h^2 Re}\big(u^n_{i+\frac{3}{2},jk} + u^n_{i-\frac{1}{2},jk} \\ &+ u^n_{i+\frac{1}{2},j+1,k} + u^n_{i+\frac{1}{2},j-1,k} + u^n_{i+\frac{1}{2},j,k+1} + u^n_{i+\frac{1}{2},j,k-1} - 6u^n_{i+\frac{1}{2},jk}\big),\end{aligned}$$

where the advection term is defined as

$$\begin{aligned}(\mathbf{u}\cdot\nabla_d u)^n_{i+\frac{1}{2},jk} = {} & u^n_{i+\frac{1}{2},jk}\bar{u}^n_{x_{i+\frac{1}{2},jk}} \\ & + \frac{v^n_{i,j-\frac{1}{2},k} + v^n_{i+1,j-\frac{1}{2},k} + v^n_{i,j+\frac{1}{2},k} + v^n_{i+1,j+\frac{1}{2},k}}{4}\bar{u}^n_{y_{i+\frac{1}{2},jk}} \\ & + \frac{w^n_{ij,k-\frac{1}{2}} + w^n_{i+1,j,k-\frac{1}{2}} + w^n_{ij,k+\frac{1}{2}} + w^n_{i+1,j,k+\frac{1}{2}}}{4}\bar{u}^n_{z_{i+\frac{1}{2},jk}}.\end{aligned} \tag{18}$$

The values $\bar{u}^n_{x_{i+\frac{1}{2},jk}}$ are computed using the following upwind scheme:

$$\bar{u}^n_{x_{i+\frac{1}{2},jk}} = \begin{cases} \dfrac{u^n_{i+\frac{1}{2},jk} - u^n_{i-\frac{1}{2},jk}}{h} & \text{if } u^n_{i+\frac{1}{2},jk} > 0, \\ \dfrac{u^n_{i+\frac{3}{2},jk} - u^n_{i+\frac{1}{2},jk}}{h} & \text{otherwise.} \end{cases} \tag{19}$$

The other values $\tilde{v}_{i,j+\frac{1}{2},k}$ and $\tilde{w}_{ij,k+\frac{1}{2}}$ are calculated similarly. Then, we solve the following equations for the advanced pressure field at the $(n+1)$-th time step.

$$\frac{\mathbf{u}^{n+1} - \tilde{\mathbf{u}}}{\Delta t} = -\nabla_d p^{n+1}, \tag{20}$$

$$\nabla_d \cdot \mathbf{u}^{n+1} = 0. \tag{21}$$

Applying the divergence operator to Eq. (20) and using Eq. (21), we have the Poisson equation for the pressure at the advanced time $(n+1)$.

$$\Delta_d p^{n+1} = \frac{1}{\Delta t} \nabla_d \cdot \tilde{\mathbf{u}}, \tag{22}$$

where

$$\Delta_d p^{n+1}_{ijk} = \frac{p^n_{i+1,jk} + p^n_{i-1,jk} + p^n_{i,j+1,k} + p^n_{i,j-1,k} + p^n_{ij,k+1} + p^n_{ij,k-1} - 6p^n_{ijk}}{h^2},$$

$$(\nabla_d \cdot \tilde{\mathbf{u}})_{ijk} = \frac{\tilde{u}_{i+\frac{1}{2},jk} - \tilde{u}_{i-\frac{1}{2},jk}}{h} + \frac{\tilde{v}_{i,j+\frac{1}{2},k} - \tilde{v}_{i,j-\frac{1}{2},k}}{h} + \frac{\tilde{w}_{ij,k+\frac{1}{2}} - \tilde{w}_{ij,k-\frac{1}{2}}}{h}.$$

Since the Poisson problem is ill-posed under the no-slip boundary condition, the adjustment step is needed for p^{n+1}. Here, we specify that p^{n+1} has zero mean.

The linear system of Eq. (22) is solved using a multigrid method [35], specifically, V-cycles using Gauss–Seidel relaxation with a tolerance of 10^{-7}. After solving the pressure field, we update $u^{n+1}_{i+\frac{1}{2},jk}$ as

$$u^{n+1}_{i+\frac{1}{2},jk} = \tilde{u}_{i+\frac{1}{2},jk} - \frac{\Delta t}{h}\left(p^{n+1}_{i+1,jk} - p^{n+1}_{ijk}\right). \tag{23}$$

The variables $v^{n+1}_{i,j+\frac{1}{2},k}$ and $w^{n+1}_{ij,k+\frac{1}{2}}$ are updated in a similar manner.

Using the updated fluid velocity $\mathbf{u}^{n+1}$, we evaluate the IB velocity $\mathbf{U}^{n+1}$ and then the new boundary position $\mathbf{X}^{n+1}$ is updated according to

$$\mathbf{U}^{n+1}_l = \sum_{i=1}^{N_x}\sum_{j=1}^{N_y}\sum_{k=1}^{N_z} \mathbf{u}^{n+1}_{ijk}\delta_h(\mathbf{x}_{ijk} - \mathbf{X}^n_l)h^3, \tag{24}$$

$$\mathbf{X}^{n+1}_l = \mathbf{X}^n_l + \Delta t \mathbf{U}^{n+1}_l \text{ for } l = 1, \ldots, N_s. \tag{25}$$

This completes one time step update.

4 Numerical Results

In this section, we describe several numerical tests for a time-dependent CR in a three-dimensional domain.

4.1 Convergence Test

We first perform a convergence test to verify of the proposed algorithm. Here, we set h to $1/32$, $1/64$, and $1/128$. The initial condition of the CR is given by

$$\mathbf{X}(s,0) = (0.5 + R\cos(2\pi s), 0.5 + R\sin(2\pi s), 0.5), \tag{26}$$

where R is the radius of the CR. In this test, we take $R = 0.25$, $L_t = 2\pi(R - t)$, $Re = 10$, $We = 1$, $\Delta t = 0.1Re \cdot h/128$, and the final time $T = 0.2441$. We set the number of CR particles as

$$N_s = \left[\frac{\|\mathbf{X}(s,0)\|}{h/m}\right],$$

where $\|\mathbf{X}(s,0)\| = \int_0^{L_t} |\partial\mathbf{X}(s,0)/\partial s| \mathrm{d}s$ is the length of $\mathbf{X}(s,0)$, m is a positive integer, and $[x]$ is Gauss' notation, i.e., the largest integer not greater than x. This equation implies that there are about m Lagrangian points in one grid cell. Unless otherwise noted, we use $m = 4$ in the followings. Let us define a numerical discrete arc length as $\|\mathbf{X}^n\| = \sum_{1\le l\le N_s} \Delta X_l^n$, where $\Delta X_l^n = |X_{l+1}^n - X_l^n|$.

Figure 2a, b show the configurations at $t = 0.1221$ and the temporal evolution of the numerical arc length of the CR and L_t with respect to time, respectively. The figures indicate that the configurations of the CR converge to a circle whose circumference is L_t and that the numerical arc lengths also converge to L_t as the number of grid points increases.

In addition, the errors between L_t and $\|\mathbf{X}^n\|$ for each CR with different spatial step sizes at $t = 0.1221$ are presented in Table 1. The result shows that our model has the first order accuracy in both time and space.

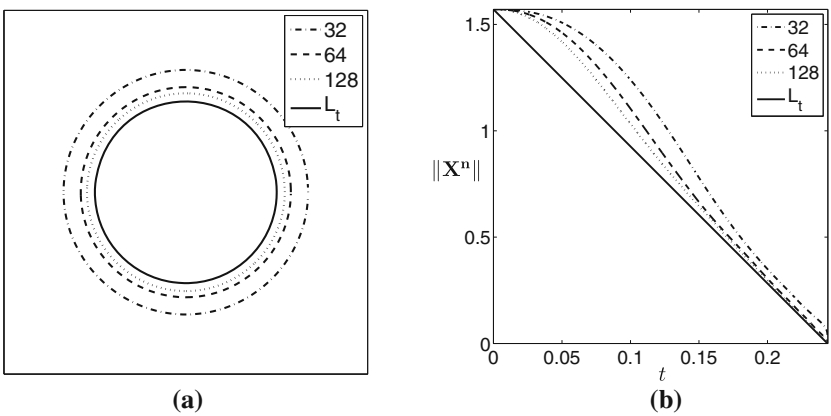

Fig. 2 **a** Configurations of CRs at $t = 0.1221$ and **b** temporal evolution of the numerical arc length $\|\mathbf{X}^n\|$ of the CR and L_t with respect to time t, respectively. $Re = 10$ and $We = 1$ are used

Table 1 Error between L_t and $\|\mathbf{X}^n\|$ for each CR with different spatial step sizes at T

h	1/32		1/64		1/128
Errors	0.2680		0.1206		0.06825
Order		1.155		0.8238	

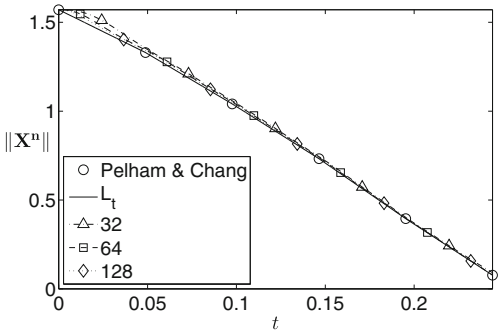

Fig. 3 $\|\mathbf{X}^n\|$ with respect to time t of CRs having different spatial step sizes

4.2 Comparison with Experimental Data

Next, a numerical simulation is conducted to show the convergence of our model to experimental data. Here, we match an unstressed length L_t with a circumference derived from a ring diameter of the wild-type one in [3]. Note that the length and time of the experimental data are non-dimensionalized by the characteristic length and time, respectively, and we take $Re = 10$ and $We = 10$. The spatial and temporal step sizes are $h = 1/32, 1/64, 1/128$, and $\Delta t = 0.1Re \cdot h/128$, respectively.

Figure 3 shows $\|\mathbf{X}^n\|$ values with respect to time t for the CRs having different spatial step sizes. The circular ($\circ$) marker represents the data in [3]. The solid line ($-$) represents L_t, which is interpolated from the experimental data. Further, the triangular (Δ), square ($\square$), and diamond ($\diamond$) markers represent the numerical results when $h = 1/32$, 1/64, and 1/128, respectively. As seen in Fig. 3, the numerical circumference converges as the mesh becomes finer and exhibits good agreement with the data from Pelham and Chang's research.

Furthermore, configurations of CRs from the numerical simulation and in vivo are presented in Fig. 4. Here, the in vivo images are generated by the reverse progress for better classification, and the solid line represents $\|\mathbf{X}^n\|$ in our model. The results demonstrate that our modeling of the CR is in good agreement with the experimental results.

4.3 Effect of the Reynolds Number

To check the effect of Re, we consider another simulation with the same initial condition as in Fig. 2 on a 64^3 mesh grid. The fixed temporal step size $\Delta t = 0.1^2h^2$, $L_t = 2\pi(R - 0.5t/T)$, $R = 0.25$, and $We = 1$ are used and the number of iterations is 4000; i.e., $T = 9.7656 \times 10^{-3}$. Figure 5 shows the temporal evolution of the numerical arc length $\|\mathbf{X}^n\|$ of the CR for $Re = 10^\gamma, \gamma = -1, \ldots, 3$ with respect to time. The result confirms that the rate of shrinkage of the CR depends on the Reynolds number.

Further, we consider a similar simulation to check the effect of Re with respect to t/T. Here, the parameters in Fig. 5 are used, except for T (or the number of iterations) and L_t, which depends on T. Figure 6 shows the temporal evolution of the numerical arc length $\|\mathbf{X}^n\|$ of the CR for various Re values with respect to the relative time t/T. The evolutions which correspond to the legends 0.1 (circle marker), 1 (diamond marker), and 10 (plus marker) are the same as in Fig. 5, whereas, the evolutions which correspond to the legends $0.1(L)$ (asterisk marker) and $10(S)$ (square marker) are obtained from a longer simulation $T = 5.8594 \times 10^{-2}$ and a shorter simulation $T = 4.3945 \times 10^{-3}$, respectively. Although each simulation has a different final time and shrinkage rate, the graphs for $0.1(L)$, 1, and $10(S)$ have a similar

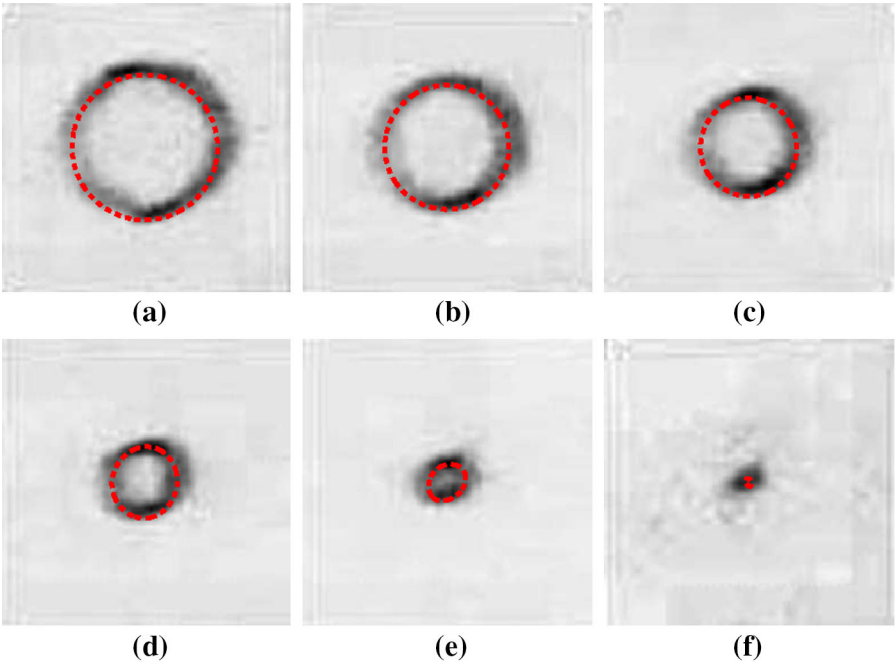

Fig. 4 Configurations of CRs from the numerical simulation and in vivo. *Background images* are reprinted with permission from Nature [3] and *dashed lines* represent our simulation results

Fig. 5 Temporal evolution of the numerical arc length $\|\mathbf{X}^n\|$ of the CR for various *Re* values with respect to time *t*

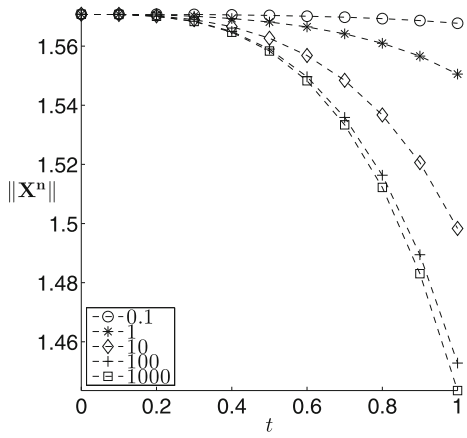

overall shape. The result implies that the effect of the Reynolds number may be precisely varied by changing the time scale and the shrinkage rate in our model.

4.4 Point-Deleting Algorithm

During temporal evolution, two adjacent points in the IB can be too close to each other. For efficient numerical calculation, we dynamically delete points whose distance from their neighboring points becomes less than a given length, α. To be more specific, let us assume that

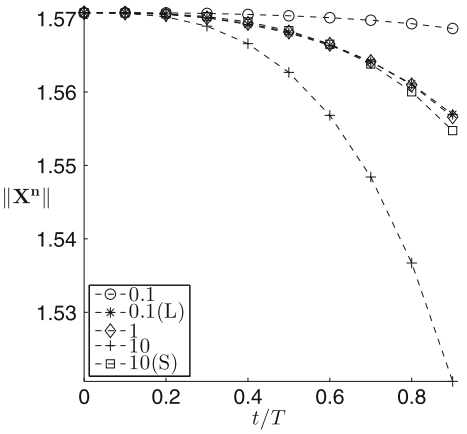

Fig. 6 Temporal evolution of the numerical arc length $\|\mathbf{X}^n\|$ of the CR for various Re values with respect to relative time t/T

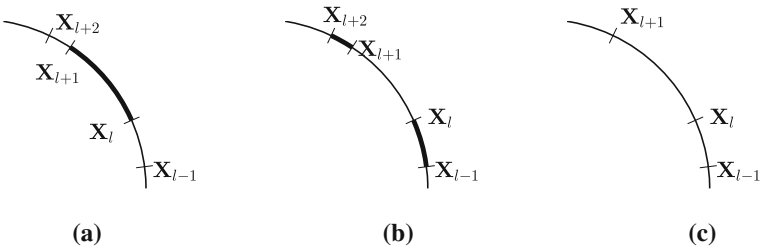

Fig. 7 Schematic of algorithm for deleting points. **a** Find an index l, **b** determine the deleted point, and **c** delete and renumber

there is an index l which satisfies $|\mathbf{X}_{l+1}^n - \mathbf{X}_l^n| < \alpha$; then we check whether $|\mathbf{X}_{l+2}^n - \mathbf{X}_{l+1}^n| \leq |\mathbf{X}_l^n - \mathbf{X}_{l-1}^n|$. If that is true, then we delete $\mathbf{X}_{l+1}^n$; otherwise, we delete $\mathbf{X}_l^n$ (see Fig. 7). At the same time, we delete the corresponding s_{l+1}^n or s_l^n. Next, we rearrange the numbering of s_l^n and $\mathbf{X}_l^n$. In this point-deleting algorithm, we make ΔX_l^n be bounded as $\alpha \leq \Delta X_l^n \leq \alpha + h/m$ for $l = 1, \ldots, N_s$ and we can avoid clustering of the IB points while the CR is shrinking.

Figure 8 shows the distribution of the maximum, minimum, and average of $\Delta X_l^n / \Delta X_l^0$ on 64^3 mesh grids with respect to time. Here, we use $\alpha = h/8$, $R = 0.25$, $L_t = 2\pi(R - t)$, $Re = 10$, $We = 1$, $\Delta t = 0.1Re/128^2$, and $T = 0.2441$ with the initial condition (26). The

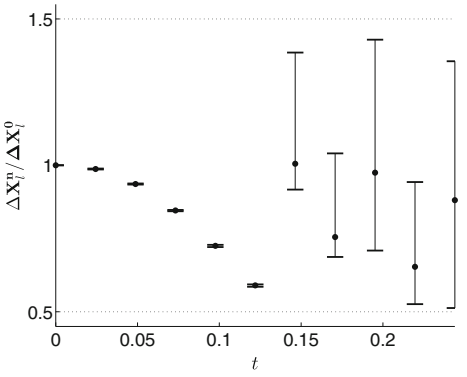

Fig. 8 Distribution of the maximum (-), minimum (-), and average (·) of $\Delta X_l^n / \Delta X_l^0$ for $l = 1, 2, \ldots, N_s$ with respect to time t

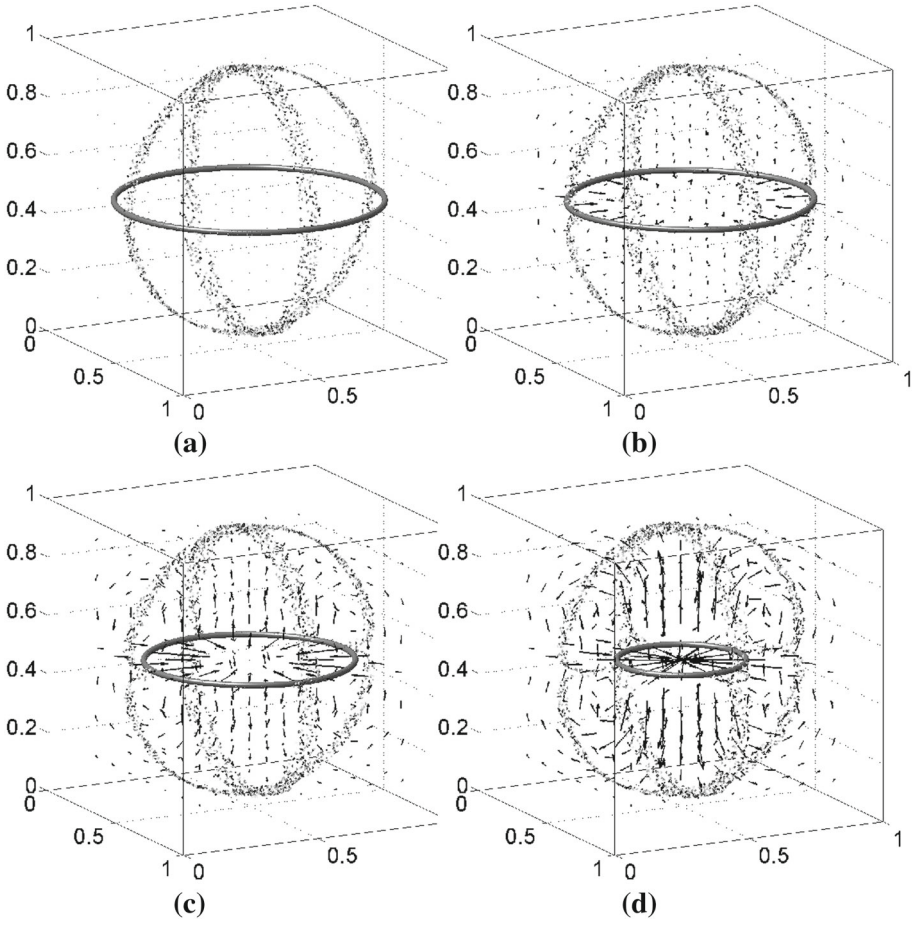

Fig. 9 CR (*solid line*), Lagrangian particles (*points*), and velocity field (*arrows*) at **a** $t = 0$, **b** $t = 0.4883$, **c** $t = 0.6836$, and **d** $t = 0.8789$. Initial positions of particles are randomly distributed in two crossed bands

dotted lines represent the upper and lower bounds of ΔX_l^n, i.e., α and $\alpha + h/m$, respectively. The result proves that the boundedness of ΔX_l^n is satisfied.

4.5 Particle Tracing

We trace Lagrangian particles that are passively advected by the velocity field to see the fluid flow generated by the CR. The initial positions of the particles are randomly distributed in two bands: one band is $\{(x, y, z)|0.46 \leq x \leq 0.54, (x-0.5)^2 + (y-0.5)^2 + (z-0.5)^2 = 0.45^2\}$ and the other is $\{(x, y, z)|0.46 \leq y \leq 0.54, (x-0.5)^2 + (y-0.5)^2 + (z-0.5)^2 = 0.45^2\}$. Here, we use $Re = 10$ and $We = 10$ on a 64^3 mesh grid. The CR (solid line), Lagrangian particles (points), and velocity field (arrows) at (a) $t = 0$, (b) $t = 0.4883$, (c) $t = 0.6836$, and (d) $t = 0.8789$ are shown in Fig. 9a–d, respectively.

We also trace the simulated particles whose initial conditions are given on the sphere with radius $R = 0.45$. Here, we also use $Re = 10$ and $We = 10$ on a 64^3 mesh grid, as in the

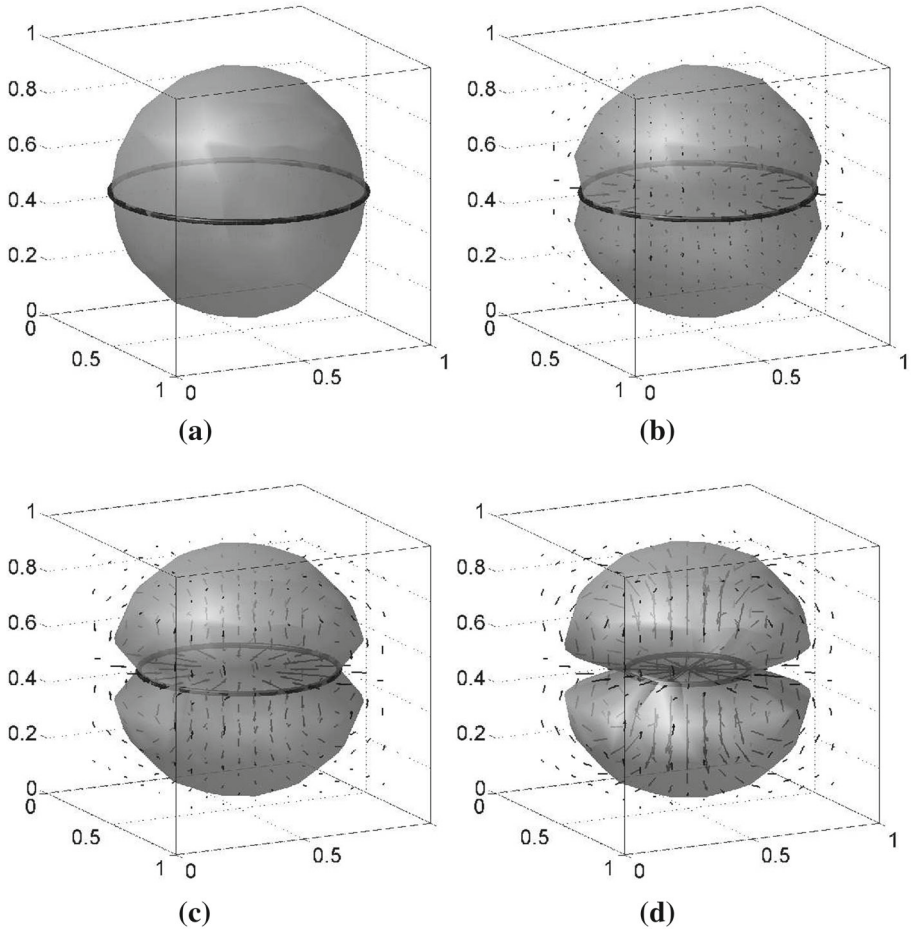

Fig. 10 CR (*solid line*), Lagrangian particles (*points*), and velocity field (*arrows*) at **a** $t = 0$, **b** $t = 0.4883$, **c** $t = 0.6836$, and **d** $t = 0.8789$. Initial positions of particles are given on the *sphere*

previous simulation. The numerical results for the CR, Lagrangian particles, and velocity field are displayed in Fig. 10. Here, the surface generated by the particles is used for better visualization.

The results in Figs. 9 and 10 both represent similar CR-driven flow and similar traces of Lagrangian particles moved by the flow. Because there is no proper governing equation for the particle advection or interparticle force, this result is not suitable for modeling the cell division process. We focus only on modeling for the CR in this paper and leave detailed and robust modeling of cell division with cell membrane movement as a future work.

Next, we present additional simulation results in Fig. 11 to check the effect of the Reynolds number on the particle tracing. The CR, Lagrangian particles, and velocity field at $t = 0.2930$ for $Re = 10$, 100, and 1000 at are displayed Fig. 11a–c, respectively. The initial conditions are those of Figs. 9 and 10 in the upper and lower panels, respectively. The other parameters are the same as in Figs. 9 and 10. Note that the results in Fig. 11 are earlier stages of those in Figs. 9b and 10b.

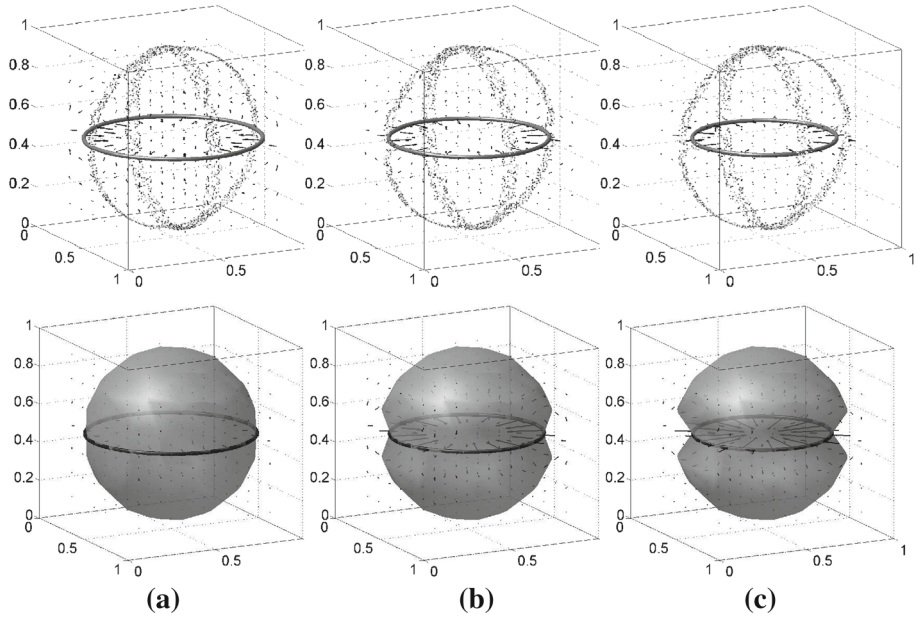

Fig. 11 CR (*solid line*), Lagrangian particles (*points*), and velocity field (*arrows*) for **a** $Re = 10$, **b** $Re = 100$, and **c** $Re = 1000$ at $t = 0.2930$

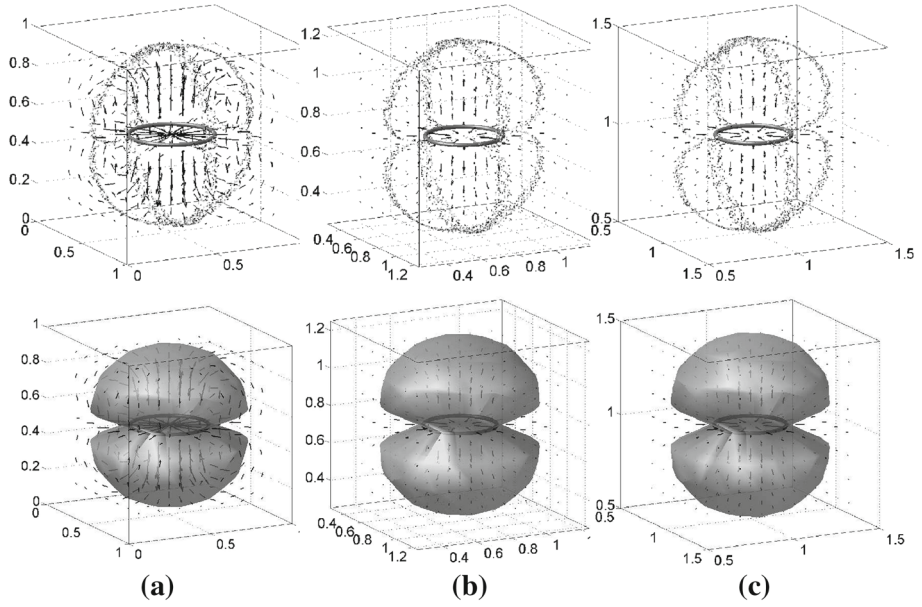

Fig. 12 CR (*solid line*), Lagrangian particles (*points*), and velocity field (*arrows*) for domain sizes of **a** $(0, 1)^3$, **b** $(0, 1.5)^3$, and **c** $(0, 2)^3$ at $t = 0.8789$

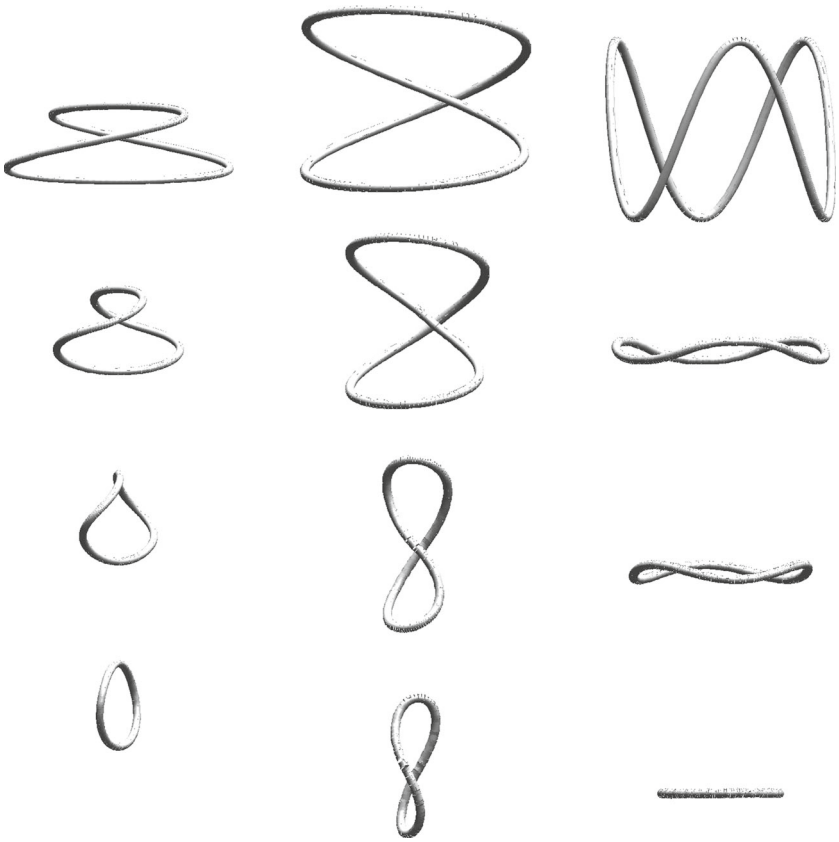

Fig. 13 Various CR configurations and their temporal evolution. *Top row* shows initial conditions. The *second*, *third*, and *fourth rows* represent the temporal evolution at $t = 0.0488$, 0.0977, and 0.1465, respectively

Finally, we perform a numerical simulation to check the effect of the domain size on the particle tracing. The domains $(0, 1)^3$ with a 64^3 meshgrid, $(0, 1.5)^3$ with a 96^3 meshgrid, and $(0, 2)^3$ with 128^3 meshgrid are considered, and the other parameters are the same as in Figs. 9 and 10. Figure 12a–c shows CR, Lagrangian particles, and velocity field with domain sizes of (a) $(0, 1)^3$, (b) $(0, 1.5)^3$, and (c) $(0, 2)^3$, respectively, at $t = 0.8789$, which is the final time in Figs. 9d and 10d. Here, the domains are partially displayed to compare the shapes of particles conveniently. The locations of particles are almost the same near the CR in each domain; however, the results show that particles are more diffused in the z-direction as the domain size increases.

4.6 Various Initial Configurations

Simulations with various initial configurations are described in this section. The computations are done on a 32^3 mesh grid, and the other parameters are the same as in the previous sections. We consider a bent and twisted ring, a twisted ring, and a bent ring as the initial conditions of the CRs:

$$\mathbf{X}_l^0 = 0.5 + (R\cos(s_l)\,,\ R\sin(2s_l)\,,\ 0.1\sin(s_l))\,,$$
$$\mathbf{X}_l^0 = 0.5 + (R\cos(2s_l)\,[0.9 + 0.1\sin(s_l)]\,,\ R\sin(2s_l)\,,\ 0.2\cos(s_l))\,,$$

$$\mathbf{X}_l^0 = 0.5 + (R\cos(s_l), R\sin(s_l), 0.2\sin(3s_l)),$$

where $R = 0.45$ and $s_l = 2\pi(l-1)/N_s$, respectively.

Figure 13 shows the various CR configurations and their temporal evolution. The initial conditions are shown in the top row. The second, third, and fourth rows represent the temporal evolution at $t = 0.0488$, 0.0977, and 0.1465, respectively. The numerical results show that the proposed method works well with more complex initial configurations than a circular ring.

Although the proposed model is motivated by the CR in cytokinesis, we expect that our model has potential for application to other phenomena in which an elastic ring undergoes contraction, such as a thin elastic ring under constraint [36], buckling [37], and mortar [38]. The simulations in this section could be useful for implementation in these other areas instead of in the cell division process.

5 Conclusion

We proposed an IB method for a contractile elastic ring in a three-dimensional Newtonian fluid. The length of the elastic ring is time dependent and decreases as time evolves. The governing equations are the modified Navier–Stokes equations with an elastic force from the contractile ring. We dynamically reduced the number of Lagrangian boundary points when the distance between adjacent points was too small. We performed numerical experiments with various initial configurations of the contractile elastic ring. The numerical results showed that the proposed method can model and simulate the time-dependent contractile elastic ring in a three-dimensional Newtonian fluid. The effects of various parameters were also investigated using numerical simulations. As a future work, we will incorporate the proposed contractile elastic ring into a model of the cell division process [39–41].

Acknowledgments The corresponding author (J.S. Kim) was supported by the National Research Foundation of Korea (NRF) grant funded by the Korea government (MSIP) (NRF-2014R1A2A2A01003683). W. Lee's work was supported by the National Institute for Mathematical Sciences (NIMS) grant funded by Korea government (No. B21402-2).

References

1. Pollard, T.D., Cooper, J.A.: Actin, a central player in cell shape and movement. Science **326**, 1208–1212 (2008)
2. Shlomovitz, R., Gov, N.S.: Physical model of contractile ring initiation in dividing cells. Biophys. J. **94**, 1155–1168 (2008)
3. Pelham, R.J., Chang, F.: Actin dynamics in the contractile ring during cytokinesis in fission yeast. Nature **419**, 82–86 (2002)
4. Jochova, J., Rupes, I., Streiblova, E.: F-actin contractile rings in protoplasts of the yeast Schizosaccharomyces. Cell Biol. Int. Rep. **15**, 607–610 (1991)
5. Chang, F., Drubin, D., Nurse, P.: cdc12p, a protein required for cytokinesis in fission yeast, is a component of the cell division ring and interacts with profilin. J. Cell Biol. **137**, 169–182 (1997)
6. Bi, E., Maddox, P., Lew, D.J., Salmon, E.D., McMilland, J.N., Yeh, E., Pringle, J.R.: Involvement of an actomyosin contractile ring in Saccharomyces cerevisiae cytokinesis. J. Cell Biol. **142**, 1301–1312 (1998)
7. Mandato, C.A., Berment, W.M.: Contraction and polymerization cooperate to assemble and close actomyosin rings round Xenopus oocyte wounds. J. Cell Biol. **154**, 785–797 (2001)
8. Celton-Morizur, S., Bordes, N., Fraisier, V., Tran, P.T., Paoletti, A.: C-terminal anchoring of mid1p to membranes stabilizes cytokinetic ring position in early mitosis in fission yeast. Mol. Cell Biol. **24**, 10621–10635 (2004)

9. Kamasaki, T., Osumi, M., Mabuchi, I.: Three-dimensional arrangement of F-actin in the contractile ring of fission yeast. J. Cell Biol. **178**, 765–771 (2007)
10. Carvalgo, A., Desai, A., Oegema, K.: Structural memory in the contractile ring makes the duration of cytokinesis independent of cell size. Cell **137**, 926–937 (2009)
11. Bathe, M., Chang, F.: Cytokinesis and the contractile ring in fission yeast: towards a systems-level understanding. Trends Microbiol. **18**, 38–45 (2010)
12. Calvert, M.E., Wright, G.D., Lenong, F.Y., Chiam, K.H., Chen, Y., Jedd, G., Balasubramanian, M.K.: Myosin concentration underlies cell size-dependent scalability of actomyosin ring constriction. J. Cell Biol. **195**, 799–813 (2011)
13. Zhou, M., Wang, Y.L.: Distinct pathways for the early recruitment of myosin II and actin to the cytokinetic furrow. Mol. Biol. Cell. **19**(1), 318–326 (2008)
14. Vavylonis, D., Wu, J.-Q., Hao, S., O'Shaughnessy, B., Pollard, T.D.: Assembly mechanism of the contractile ring for cytokinesis by fission yeast. Science **319**, 97–100 (2008)
15. Zhou, Z., Munteanu, E.L., He, J., Ursell, T., Bathe, M., Huang, K.C., Chang, F.: The contractile ring coordinates curvature-dependent septum assembly during fission yeast cytokinesis. Mol. Biol. Cell **26**(1), 78–90 (2015)
16. Peskin, C.S.: Flow patterns around heart valves: a numerical method. J. Comput. Phys. **10**(2), 252–271 (1972)
17. Peskin, C.S.: Numerical analysis of blood flow in the heart. J. Comput. Phys. **25**, 220–252 (1997)
18. Peskin, C.S.: The immersed boundary method. Acta Numerica **1**, 479–517 (2002)
19. Bigot, B., Bonometti, T., Lacaze, L., Thual, O.: A simple immersed-boundary method for solid-fluid interaction in constant- and stratified-density flows. Comput. Fluids **97**, 126–142 (2014)
20. Chang, P., Liao, C., Hsu, H., Liu, S., Lin, C.: Simulations of laminar and turbulent flows over periodic hills with immersed boundary method. Comput. Fluids **92**, 233–243 (2014)
21. Cockburn, M., Solano, M.: Solving convection–diffusion problems on curved domains by extensions from subdomains. J. Sci. Comput. **59**, 512–543 (2014)
22. De Rosis, A., Ubertini, S., Ubertini, F.: A comparison between the interpolated bounce-back scheme and the immersed boundary method to treat solid boundary conditions for laminar flows in the lattice Boltzmann framework. J. Sci. Comput. **61**, 477–489 (2014)
23. Hsieh, P.-W., Lai, M.-C., Yang, S.-Y., You, C.-S.: An unconditionally energy stable penalty immersed boundary method for simulating the dynamics of an inextensible interface interacting with a solid particle. J. Sci. Comput. **64**, 289–316 (2015)
24. Lim, S., Ferent, A., Wang, X.S., Peskin, C.S.: Dynamics of a closed rod with twist and bend in fluid. SIAM J. Sci. Comput. **31**(1), 273–302 (2008)
25. Lim, S.: Dynamics of an open elastic rod with intrinsic curvature and twist in a viscous fluid. Phys. Fluids **22**(2), 024104 (2010)
26. Vahidkhah, K., Abdollahi, V.: Numerical simulation of a flexible fiber deformation in a viscous flow by the immersed boundary-lattice Boltzmann method. Commun. Nonlinear Sci. **17**(3), 1475–1484 (2012)
27. Chen, Z.L., Hickel, S., Devesa, A., Berland, J., Adams, N.A.: Wall modeling for implicit large-eddy simulation and immersed-interface methods. Theor. Comput. Fluid Dyn. **28**(1), 1–21 (2014)
28. Posa, A., Balaras, E.: Model-based near-wall reconstructions for immersed-boundary methods. Theor. Comput. Fluid Dyn. **28**(4), 473–483 (2014)
29. Botella, O., Ait-Messaoud, M., Pertat, A., Cheny, Y., Rigal, C.: The LS-STAG immersed boundary method for non-Newtonian flows in irregular geometries: flow of shear-thinning liquids between eccentric rotating cylinders. Theor. Comput. Fluid Dyn. **29**, 93–110 (2015)
30. Zhang, N., Zheng, Z.C.: An improved direct-forcing immersed-boundary method for finite difference applications. J. Comput. Phys. **221**(1), 250–268 (2007)
31. Rosar, M.E., Peskin, C.S.: Fluid flow in collapsible elastic tubes: a three-dimensional numerical model. N. Y. J. Math. **7**, 281–302 (2001)
32. Harlow, E., Welch, J.: Numerical calculation of time dependent viscous incompressible flow with free surface. Phys. Fluids **8**, 2182–2189 (1965)
33. Chorin, A.J.: Numerical solution of the Navier–Stokes equation. Math. Comput. **22**(104), 745–762 (1968)
34. Lai, M.C., Peskin, C.S.: An immersed boundary method with formal second-order accuracy and reduced numerical viscosity. J. Comput. Phys. **160**, 705–719 (2000)
35. Trottenberg, U., Oosterlee, C., Schüller, A.: Multigrid. Academic Press, London (2001)
36. Bottega, W.J.: On the constrained elastic ring. J. Eng. Math. **24**, 43–51 (1988)
37. El-Bayoumy, L.: Buckling of a circular elastic ring confined to a uniformly contracting circular boundary. J. Appl. Math. **39**(3), 758–766 (1972)
38. Choi, H., Lim, M., Kitagaki, R., Noguchi, T., Kim, G.: Restrained shrinkage behavior of expansive mortar at early ages. Constr. Build. Mater. **84**(1), 468–476 (2015)

39. Li, Y., Yun, A., Kim, J.: An immersed boundary method for simulating a single axisymmetric cell growth and division. J. Math. Biol. **65**(4), 653–675 (2012)
40. Rejniak, K.A.: An immersed boundary framework for modelling the growth of individual cells: an application to the early tumour development. J. Theor. Biol. **247**(1), 186–204 (2007)
41. Rejniak, K.A., Dillon, R.H.: A single cell-based model of the ductal tumour microarchitecture. Comput. Math. Methods Med. **8**(1), 51–69 (2007)